IEEE Journal of Microwaves

Received 30 June 2024; revised 15 August 2024; accepted 23 August 2024. Date of publication 20 September 2024; date of current version 9 October 2024.

Digital Object Identifier 10.1109/JMW.2024.3453325

Ordinary and Extraordinary Permittivities of 4H SiC at Different Millimeter-Wave Frequencies, Temperatures, and Humidities

TIANZE LI [1,2] (Student Member, IEEE), LEI LI [1,2] (Member, IEEE), XIAOPENG WANG [1,2] (Member, IEEE), JAMES C. M. HWANG [1,2] (Life Fellow, IEEE), SHANA YANAGIMOTO [3], AND YOSHIYUKI YANAGIMOTO [3]

(Regular Paper)

[1]Department of Materials Science and Engineering, Cornell University, Ithaca, NY 14853 USA
[2]School of Electrical and Computer Engineering, Cornell University, Ithaca, NY 14853 USA
[3]EM labs, Inc., Kobe, Hyogo 653-0842, Japan

CORRESPONDING AUTHOR: Tianze Li (e-mail: tl762@cornell.edu).

This work was supported in part by the U.S. National Science Foundation under Grant ECCS-2117305 and Grant ECCS-2132323, in part by the U.S. Department of Defense through the State of the Art Radio Frequency Gallium Nitride Program, in part by the U.S. Army Research Office under Grant W911NF2410023, and in part by the Semiconductor Research Corporation and the U.S. Defense Advanced Research Projects Agency through the Joint University Microelectronics Program.

ABSTRACT Hexagonal semiconductors such as 4H SiC have important high-frequency, high-power, and high-temperature applications. The applications require accurate knowledge of both ordinary and extraordinary relative permittivities, $\varepsilon_\perp$ and $\varepsilon_\parallel$, perpendicular and parallel, respectively, to the c axis of these semiconductors. However, due to challenges for suitable test setups and precision high-frequency measurements, little reliable data exists for these semiconductors especially at millimeter-wave frequencies. Recently, we reported $\varepsilon_\parallel$ of 4H SiC from 110 to 170 GHz. This paper expands on the previous report to include both $\varepsilon_\perp$ and $\varepsilon_\parallel$ of the same material from 55 to 330 GHz, as well as their temperature and humidity dependence enabled by improving the measurement precision to two decimal points. For example, at room temperature, real $\varepsilon_\perp$ and $\varepsilon_\parallel$ are constant at 9.77 ± 0.01 and 10.20 ± 0.05, respectively. By contrast, the ordinary loss tangent increases linearly with the frequency f in the form of $(4.9 \pm 0.1) \times 10^{-16} f$. The loss tangent, less than 1×10^{-4} over most millimeter-wave frequencies, is significantly lower than that of sapphire, our previous low-loss standard. Finally, both $\varepsilon_\perp$ and $\varepsilon_\parallel$ have weak temperature coefficients on the order of 10^{-4} /°C. The knowledge reported here is especially critical to millimeter-wave applications of 4H SiC, not only for solid-state devices and circuits, but also as windows for high-power vacuum electronics.

INDEX TERMS Dielectric constant, millimeter wave, substrate integrated waveguide, Fabry–Perot resonator, loss tangent, permittivity, silicon carbide.

I. INTRODUCTION

In addition to optoelectronic applications, 4H SiC is widely used in high-power and high-frequency applications [1]. For example, high-power GaN high-electron mobility transistors (HEMTs) are usually fabricated on epitaxial layers grown on high-purity semi-insulating (HPSI, $\geq 10^7$ Ω·cm) c-axis 4H-SiC substrates. In turn, the HEMTs are interconnected with high-frequency signals through microstrip or coplanar transmission lines directly fabricated on the SiC substrate. In these transmission lines, the signals travel in the quasi-transverse-electromagnetic (quasi-TEM) mode governed by both the ordinary permittivity $\varepsilon_\perp$ and the extraordinary permittivity $\varepsilon_\parallel$, perpendicular and parallel, respectively, to the c axis (Fig. 1) [2]. By contrast, for the transverse-electric (TE) wave propagating in a substrate-integrated waveguide (SIW) fabricated along the c plane, the field is always parallel to the c axis, hence only governed by $\varepsilon_\parallel$ [3].

In general, the complex permittivity ε is defined as

$$\varepsilon = \varepsilon_0 \varepsilon_R = \varepsilon_0 \left(\varepsilon'_R - j\varepsilon''_R\right) = \varepsilon_0 \varepsilon'_R \left(1 - j \tan\delta\right), \quad (1)$$

where ε_0 is the vacuum permittivity, ε_R is the relative permittivity $\varepsilon_\perp$ or $\varepsilon_\parallel$, and $\tan\delta$ is the loss tangent. If $\tan\delta << 1$, $\varepsilon_R \approx \varepsilon'_R$.

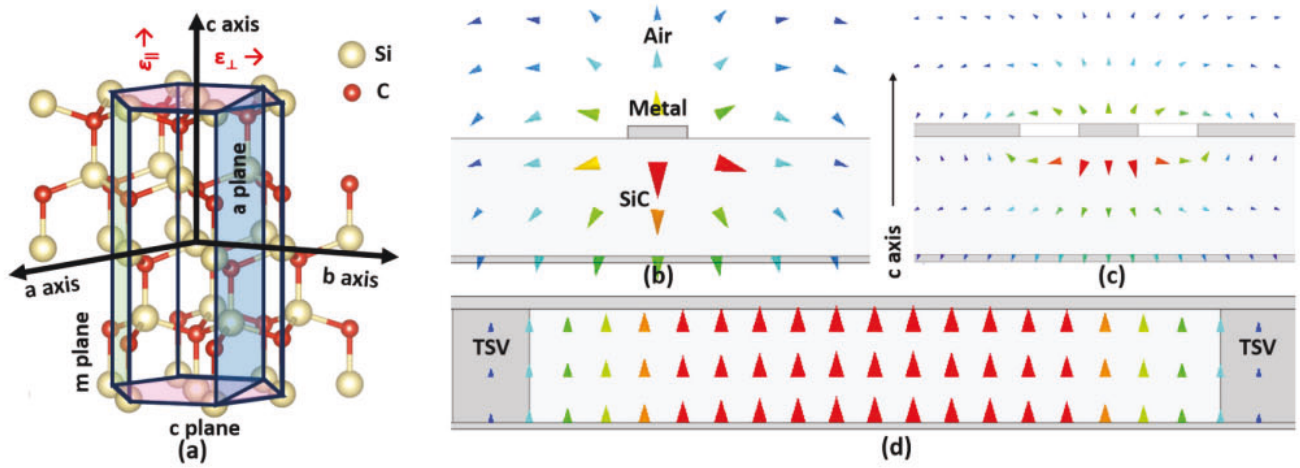

FIGURE 1. (a) Crystal structure of 4H SiC [2] and simulated electric field distributions in a cross section along the c axis of (b) a microstrip transmission line, (c) a coplanar transmission line, and (d) a substrate-integrated waveguide with through-substrate vias (TSVs), all fabricated on the c plane. Arrows point to field directions. The larger the arrow, the higher the field.

A millimeter plane wave of power P_0, after propagating for x distance in a low-loss nonmagnetic material characterized by ε, is attenuated according to the attenuation constant α and delayed according to the phase constant β [3]. Thus,

$$P(x) = P_0 \exp(-\alpha x) \exp(-j\beta x), \tag{2}$$

and

$$\alpha = \frac{\omega}{c}\sqrt{\frac{\varepsilon_R}{2}\left(\sqrt{1+\tan^2\delta}-1\right)} \approx \frac{\omega}{2c}\sqrt{\varepsilon_R \tan\delta}, \tag{3}$$

$$\beta = \frac{\omega}{c}\sqrt{\frac{\varepsilon_R}{2}\left(\sqrt{1+\tan^2\delta}+1\right)} \approx \frac{\omega}{c}\sqrt{\varepsilon_R}, \tag{4}$$

where $\omega = 2\pi f$ is the angular frequency, c is the speed of light in vacuum, and $\tan\delta << 1$.

In measurement systems with a characteristic impedance of 50 Ω, the attenuation can also be related to the insertion loss IL and the transmission coefficient S_{21} by

$$-IL(x) = 10 \cdot \log|S_{21}|^2 = 10 \cdot \log\frac{P(x)}{P_0} = 10 \cdot \log e^{-\alpha x}, \tag{5}$$

where the minus sign makes IL positive.

However, measuring these permittivities by conventional techniques is challenging especially at millimeter-wave frequencies. As the result, there is little data for $\varepsilon_\parallel$, whereas $\varepsilon_\perp$ obtained by different labs and techniques can differ by as much as 10% [Fig. 2(a)] [4], [5], [6], [7], [8], [9], [10]. Some of the data also exhibit non-physical dispersions, likely due to measurement artifacts. Lacking measurement precision, the minimum tan δ reported is often on the order of 0.001 [5]. Finally, there is no report for the temperature or humidity dependence of permittivities at millimeter-wave frequencies, despite applications in a harsh environment.

Recently, using SIWs fabricated along the c plane of HPSI 4H SiC, we reported $\varepsilon_\parallel$ across the D band (110–170 GHz)

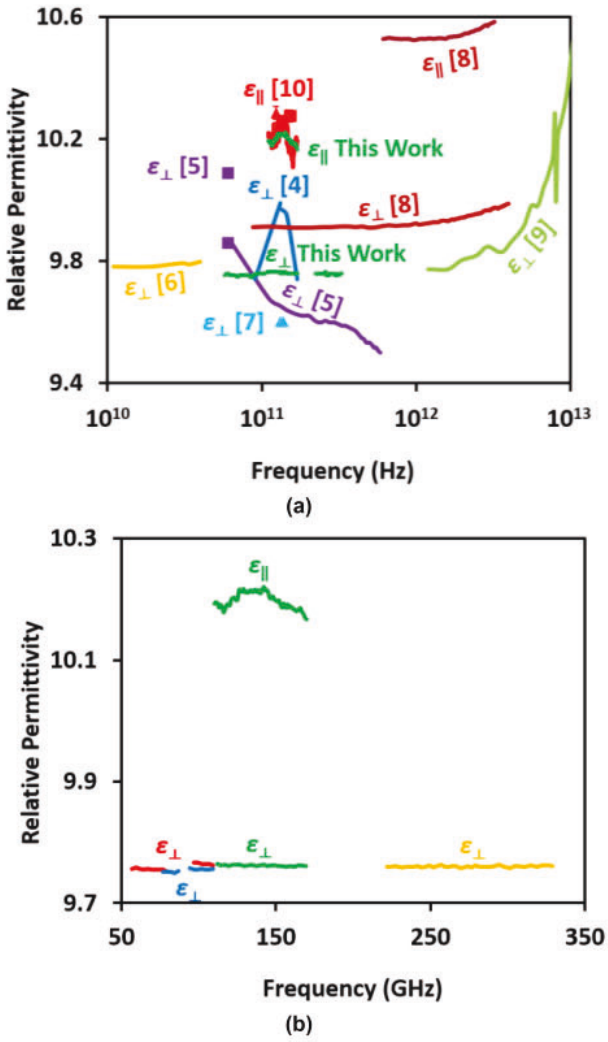

FIGURE 2. (a) Relative ordinary permittivity $\varepsilon_\perp$ and extraordinary permittivity $\varepsilon_\parallel$ of 4H SiC at room temperature [4], [5], [6], [7], [8], [9], [10]. (b) Expanded scales for $\varepsilon_\perp$ and $\varepsilon_\parallel$ of this work.

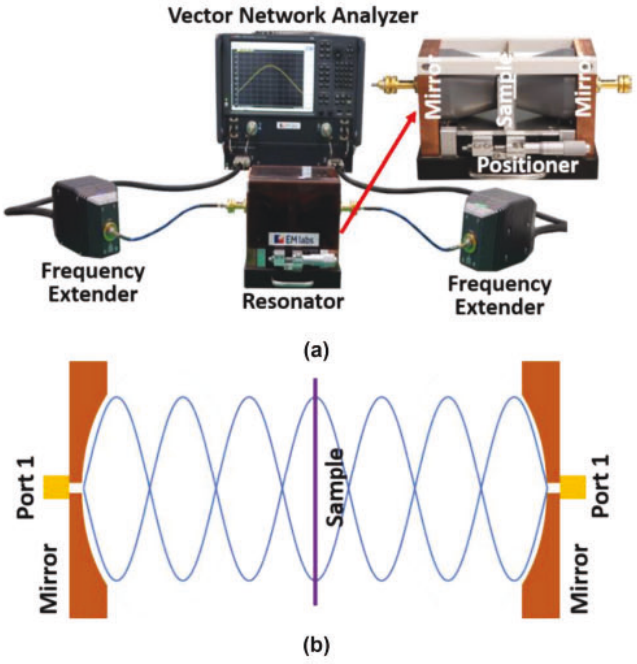

FIGURE 3. (a) Setup for measuring $\varepsilon_\perp$ on a fabry-perot open-air resonator (detailed in inset). (b) Schematics of a standing wave with 7 anti-nodes in the Fabry-Perot resonator.

[Fig. 2(a)] [10]. In this paper, we report more precise values of $\varepsilon_\parallel$, as well as $\varepsilon_\perp$ measured by placing the same material in Fabry-Perot resonators (Fig. 3). In these resonators, the vertically polarized TEM wave incidents along the c axis of 4H SiC so that it is only governed by $\varepsilon_\perp$. The improved measurement precision allows us to resolve not only the difference between $\varepsilon_\perp$ and $\varepsilon_\parallel$, but also the relatively weak temperature and humidity dependence of $\varepsilon_\perp$ and $\varepsilon_\parallel$.

The measured $\varepsilon_\perp$ has been included in Fig. 2. It can be seen that $\varepsilon_\perp = 9.77 \pm 0.01$ with excellent repeatability and little dispersion between 55 and 330 GHz unlike previous reports at the same frequencies [4], [5]. The present results show that $\varepsilon_\perp$ is significantly lower than $\varepsilon_\parallel$, so that their difference can hardly be ignored. The ratio $\varepsilon_\perp/\varepsilon_\parallel \approx 0.95$ is comparable to that reported for HPSI 4H SiC at terahertz frequencies [8]. The following are details of the measurement techniques that result in unprecedented precision and repeatability without measurement artifacts, allowing permittivity values to be obtained with three-digit precision and a small standard deviation.

II. MESUREMENT

A. SAMPLE

In this work, $\varepsilon_\perp$ is measured on the same batch of wafers previously characterized [10]. It is an HPSI 4H SiC 100-cm-diameter wafer supplied by PAM-Xiamen and thinned by Rokko Electronics to a thickness $t = 98$ μm with an average surface roughness of 2 nm. The wafer orientation is within 0.1° of the c axis. The micropipe density is less than 10 cm^{-2}. The wafer bow and warp are both less than 10 μm. The wafer is divided into four quarters: the first and second quarters are measured in this work; the third and fourth quarters are saved for other uses. The quarters are too small for measurement in a broadband Fabry-Perot resonator below 55 GHz, even though the resonator can cover frequencies as low as 25 GHz. In the future, round wafers of the proper size can be used to lower the frequency range.

B. MEASUREMENT OF ORDINARY PERMITTIVITY

For measuring $\varepsilon_\perp$, Fig. 3(a) shows the setup consisting of a vector network analyzer (Keysight N5290A PNA 10 MHz–110 GHz) in conjunction with a Fabry-Perot resonator (EM labs) and two frequency extenders (Virginia Diodes) to cover different millimeter-wave bands. Four different sets of resonators and frequency extenders are used: broadband (25–110 GHz), W band (75–110 GHz), D band (110–170 GHz), and J band (220–330 GHz). The broadband and W-band sets, with their overlapping frequencies, are used to check the consistency of the measurements.

Fig. 3(b) shows schematically a Fabry-Perot resonator with its air cavity bound by two copper concave mirrors each having a radius of curvature $r = 9.6$ cm. The high conductivity of copper ensures high reflectivity. Although the reflectivity slightly decreases as the frequency increases, the high conductivity of copper makes this reduction negligible. To excite TEM waves and to detect resonances, at the center of each mirror is a loop antenna for broadband or a waveguide coupling for the W, D and J bands. With the distance between the mirrors $d = 12$ cm, resonances occur at

$$f_N = N f_0 + \left(1/\pi\right) \arccos\left(d/r - 1\right), \tag{6}$$

where $N = 1, 2, 3 \ldots, f_0 = c/2d = 1.25$ GHz, and the last term of (6) is approximately 1.45 GHz. Solving (6) for $f_N = 55$–330 GHz, $N = 45$–265. Only resonances of odd Ns are used to ensure the sample, positioned at the center of the cavity, is subject to the maximum instead of the minimum electric field.

From the magnitude of the transmission coefficient S_{21} measured across a resonator, f_N and Q_N are extracted where $Q_N = f_N/BW$ and BW is the 3-dB bandwidth of the resonance [Fig. 4(a)]. The quality factor of the resonance $Q_N = (2 \pm 1) \times 10^5$ at all millimeter-wave frequencies, allowing $\tan\delta_\perp$ to be measured down to the 10^{-5} range. Usually, Q_N is so high that it is not affected by the raw frequency response of the PNA without a 2-port calibration. The bandwidth of the intermediate frequency and the number of averaging used by the PNA are optimized for measurement speed while maintaining a sufficient signal-to-noise ratio. When a sample is inserted in the middle of the resonator, f_N and Q_N shift lower to f'_N and Q'_N. Using the micrometer of the sample positioner shown in Fig. 3(a), the sample position is finetuned to maximize the shift. This results in excellent repeatability. Fig. 4(b) shows that $\varepsilon_\perp$ and $\tan\delta_\perp$ extracted from the measured f'_N and Q'_N are highly repeatable even after the same sample is repeatedly removed from the resonator, flipped and placed back.

All measurements are performed under 23 ± 0.5 °C and 27 ± 1% relative humidity unless otherwise noted. For temperature- and humidity-dependent measurements, a special split-cylinder resonator is used to overcome the limit

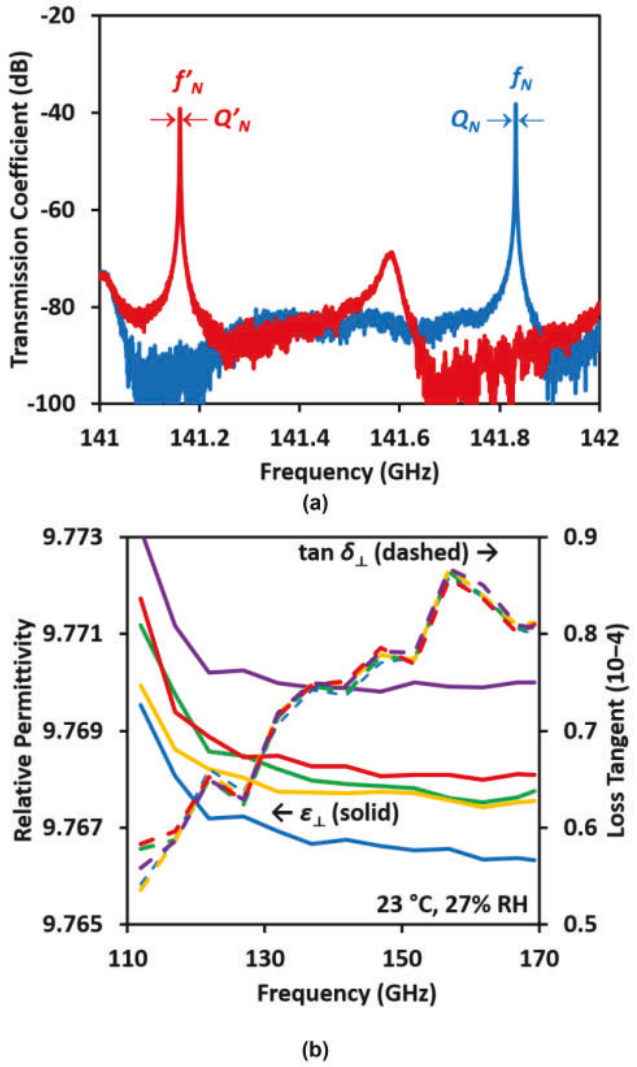

FIGURE 4. (a) Typical transmission coefficients measured on a D-band resonator before (f_N, Q_N) and after (f'_N, Q'_N) 98-μm-thick HPSI 4H SiC is inserted in the middle of a D-band Fabry-Perot resonator. (b) Relative permittivity $\varepsilon_\perp$ and loss tangent tan $\delta_\perp$ extracted from five repeated measurements on the same sample, each time with the sample removed, flipped, and placed back.

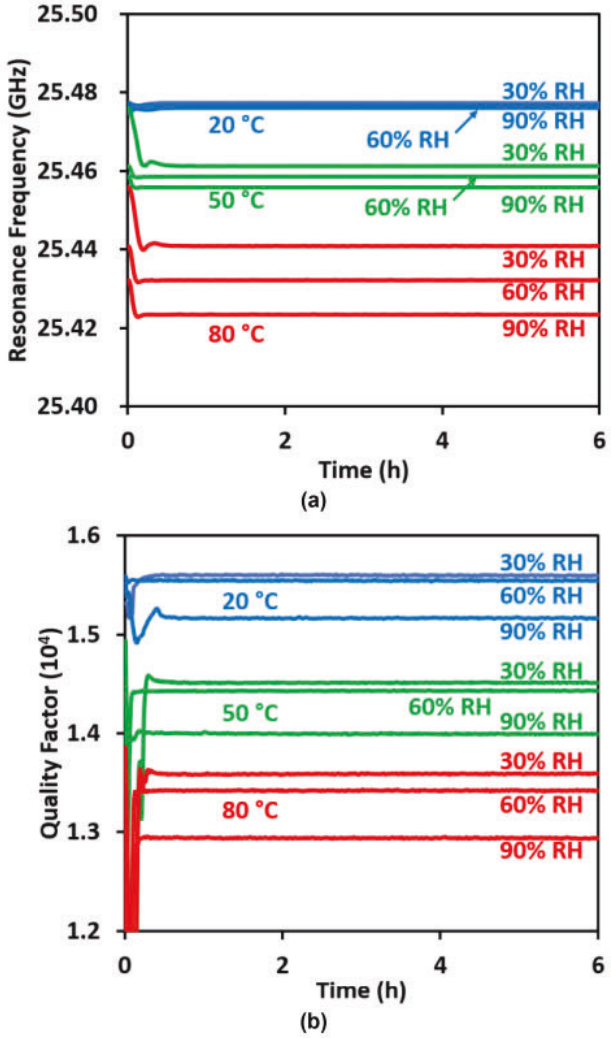

FIGURE 5. Transients in (a) resonance frequency f'_N and (b) quality factor Q'_N after a new temperature or humidity setting is applied to the same HPSI 4H SiC sample.

of the sample size for measurements below 55 GHz. This 28-GHz narrowband resonator is equipped with precise temperature and humidity control. It usually takes less than an hour for the sample to stabilize at a new temperature or humidity setting [Fig. 5]. For extra precaution, we let the sample stabilize for at least six hours at a new temperature or humidity setting before recording its steady-state $\varepsilon_\perp$ and tan $\delta_\perp$.

The measured f'_N can be used to extract $\varepsilon_\perp$ by numerically solving [11]

$$\cot\left(nkt/2-\varphi_T\right)=n\tan\left[k\left(d-t\right)/2-\varphi_D\right], \tag{7}$$

where w, φ_T and φ_D are the waist size and phase shifts of the Gaussian beam and

$$n^2=\varepsilon_\perp, \tag{8}$$

$$k=2\pi f'_N/c, \tag{9}$$

$$\varphi_T=\arctan\left(t/nkw^2\right), \tag{10}$$

$$\varphi_D=\arctan\left(\frac{d-t+t/n^2}{kw^2}\right)-\arctan\left(\frac{t}{n^2kw^2}\right), \tag{11}$$

$$\left(kw^2\right)^2=\left(d-t+t/n^2\right)\left(2r-d+t-t/n^2\right). \tag{12}$$

The measured Q'_N can be used to extract tan $\delta_\perp$ by solving [11]

$$\tan\delta_\perp=\left(\frac{1}{Q_N{}'}-\frac{1}{Q_N}\right)\left\{\frac{d+(\Delta-1)t}{\Delta t+\frac{\sin[k(d-t)-2\varphi_D]}{k}}\right\}, \tag{13}$$

where

$$\Delta=\frac{1}{\sin^2\left(2nkt-\varphi_T\right)+\left(1/n^2\right)\cos^2\left(2nkt-\varphi_T\right)}. \tag{14}$$

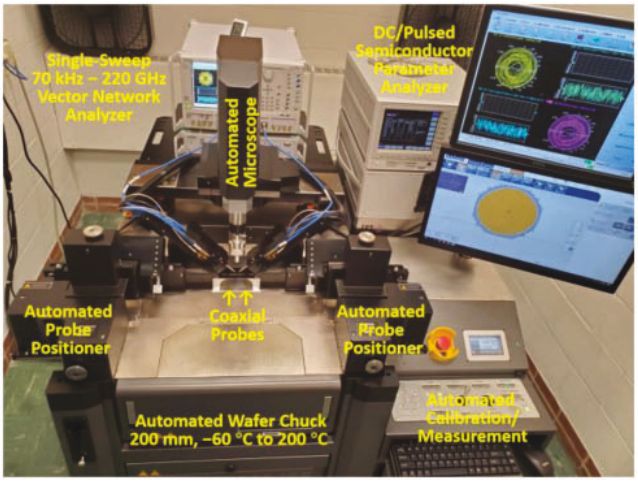

FIGURE 6. Setup for measuring $\varepsilon_{\parallel}$ on a substrate-integrated waveguide.

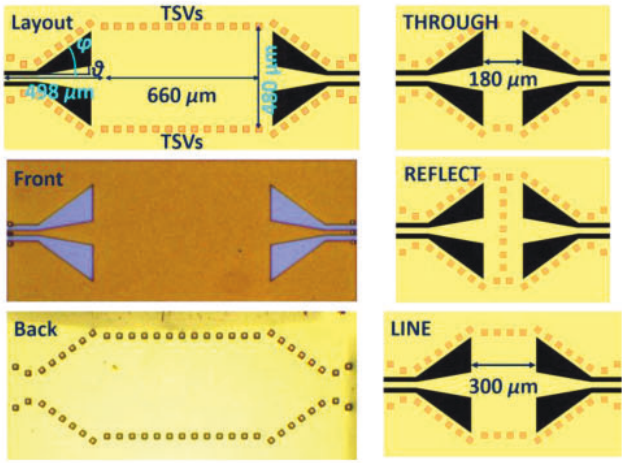

FIGURE 7. (a) Layout, frontside micrograph, and backside micrograph of a 660-μm-long substrate-integrated waveguide (SIW) sandwiched between two SIW-CPW transitions. (b) Layouts of SIW-based impedance standards through, reflect, and line.

From (13), had Q_N or Q'_N been lower than 10^5, it would have been impossible to measure $\tan\delta_{\perp}$ down to the 10^{-5} range because the f_N and f'_N resonances would have overlapped making it impossible to determine Q_N or Q'_N.

C. MEASUREMENT OF EXTRAORDINARY PERMITTIVITY

The same as in the previous measurement of $\varepsilon_{\parallel}$ [10], Fig. 6 shows the setup is based on probing an SIW on an MPI TS2000-IFE fully-automated probe station using two MPI TITAN 220-GHz 0.6-mm-diameter coaxial probes with 50-μm pitches and an Anritsu ME7838G 70-kHz-to-220-GHz vector network analyzer. The probe station can control the sample temperature from −60 °C to 200 °C with 1 °C precision.

Fig. 7(a) illustrates the layout of an SIW of length $L = 660$ μm and width $W = 480$ μm. The TE wave in the SIW is bound by top and bottom ground planes, as well as a row of through-substrate vias (TSVs) on each side. Each TSV has a square cross section of $U^2 = (30\ \mu\text{m})^2$. In each row, the TSVs are spaced with $V = 60$ μm center-to-center. To facilitate wafer probing, the SIW input and output are each transitioned to a coplanar waveguide (CPW) [12]. Each SIW-CPW transition is 498-μm long, including a 150-μm CPW section, a 258-μm tapered section, and a 90-μm SIW section. In the CPW section, the center electrode is 25-μm wide with a 25-μm gap between the center electrode and the ground electrodes. In the tapered section, the center electrode is linearly widened to 114 μm while the gap is linearly widened to 170 μm, corresponding to $\theta = 10°$ and $\varphi = 36°$ for the inner and outer angles, respectively. The SIWs are fabricated by HRL on 50-μm-thick HPSI 4H SiC using the T3 GaN-on-SiC 40-nm HEMT technology.

Scattering (S) parameters are measured across the D band on the fabricated SIWs. The as-measured S parameters are de-embedded past the CPW-SIW transitions to the intrinsic SIW section using the through-reflect-line calibration method [13], and SIW-based impedance standards THROUGH, LINE, and REFLECT fabricated together with the SIWs on the same SiC substrate [Fig. 7(b)]. With the CPW-SIW transitions and the associated $\varepsilon_{\perp}$ effects removed, the de-embedded S parameters of the 660-μm-long intrinsic SIW section depend on $\varepsilon_{\parallel}$ only. Fig. 8 shows the de-embedded reflection coefficient S_{11} and transmission coefficient S_{21}. With $|S_{11}|^2 < -20$ dB, the mismatch loss is negligible so that S_{21} is dominated by the propagation loss. However, the small $|S_{11}|^2$ results in large uncertainties in $\angle S_{11}$ as indicated by the wide shaded band in Fig. 8(b). In comparison, the uncertainty in $\angle S_{21}$ is not visible.

From the phase of the de-embedded S_{21} and the SIW length L, β can be calculated. Then, $\varepsilon_{\parallel}$ can be calculated according to [14]

$$\varepsilon_{\parallel} = \left[\left(\pi / W_{EFF}\right)^2 + \beta^2\right]\left(300/\omega\right)^2, \tag{15}$$

where W_{EFF} is the effective SIW width calculated according to [15]

$$W_{EFF} = W - \left(1.08/V - 0.1/W\right)U_{EFF}^2, \tag{16}$$

and U_{EFF} is the effective TSV diameter calculated according to

$$U_{EFF} = 2\sqrt{U^2/\pi}. \tag{17}$$

Thus, $W_{\text{EFF}} = 461$ μm and $U_{\text{EFF}} = 34$ μm. Equation (15) instead of (4) is used to account for the confinement of a waveguide. From the magnitude of the de-embedded S_{21}, $\tan\delta_{\parallel}$ can be calculated according to (5).

III. RESULTS AND DISCUSSION

Fig. 9(a) shows the measured $\tan\delta_{\perp}$ from 55 and 330 GHz. It can be seen that $\tan\delta_{\perp}$ increases linearly with frequency so that, with a coefficient of determination $R^2 > 0.96$, $\tan\delta_{\perp} = (4.9 \pm 0.1) \times 10^{-16}\, f$, where f is the frequency in Hz. It will be interesting to verify this trend by measuring $\tan\delta_{\perp}$

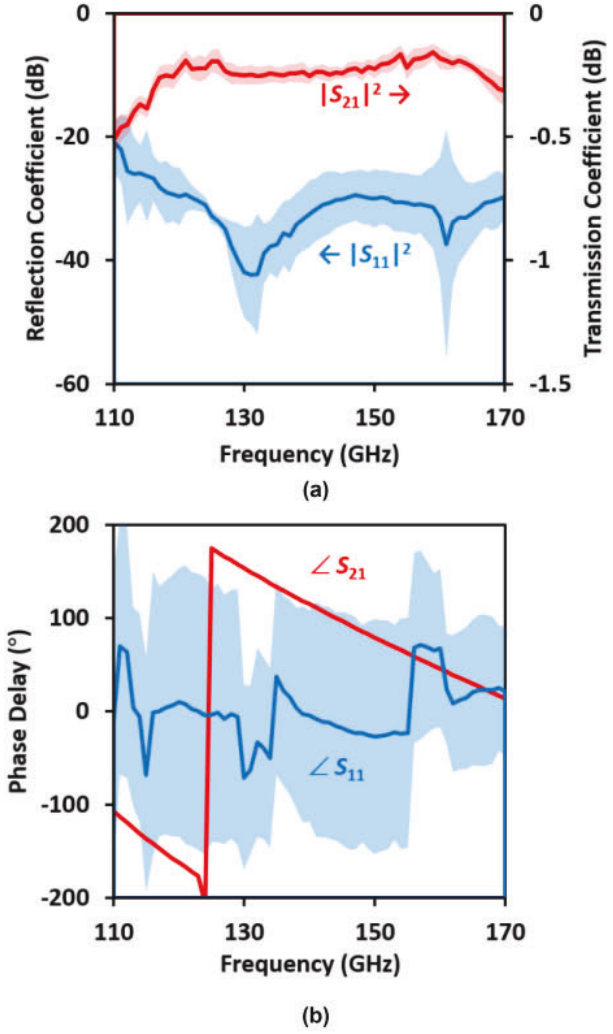

FIGURE 8. De-embedded (a) magnitudes and (b) phases of the reflection coefficient S_{11} and the transmission coefficient S_{21} of the intrinsic SIW across the D band. Shades indicate standard deviations.

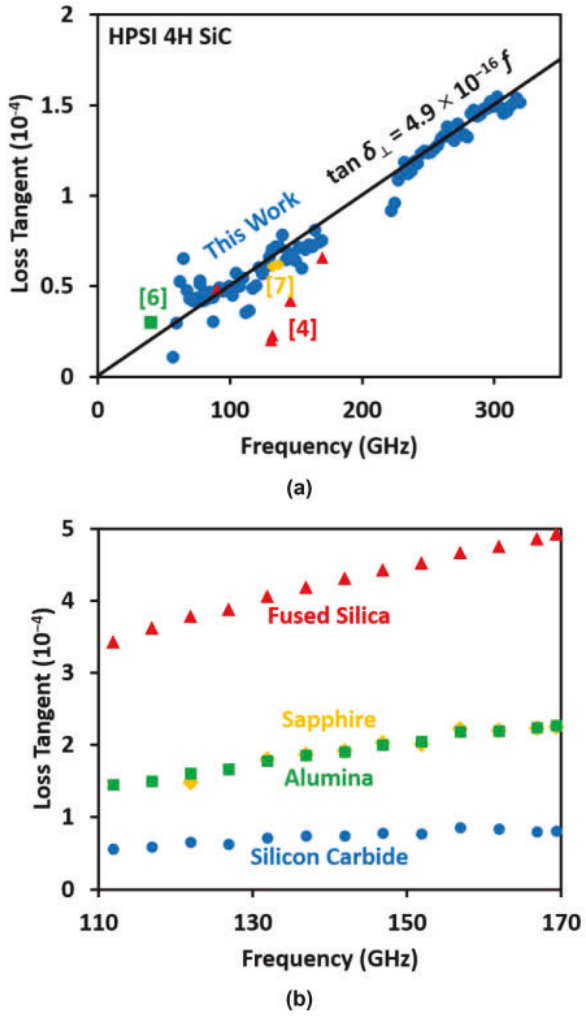

FIGURE 9. (a) Ordinary loss tangent tan $\delta_\perp$ measured across different millimeter-wave bands. (b) Comparison of loss tangents of 4H SiC, alumina, sapphire and fused silica across the D band.

below 55 GHz and see if it is even lower than 10^{-5}. However, it will require a Fabry-Perot resonator with a quality factor $Q > 10^5$, which is mechanically challenging. The present tan $\delta_\perp$ values generally agree with other reports for the loss of HPSI 4H SiC [4], [6], [7] as shown in Fig. 9(a). However, our data extend the frequency to 330 GHz with a consistently linear dependence on frequency.

The value of tan $\delta_\perp = 3 \times 10^{-5}$ at 60 GHz is the lowest we have measured on any solid as shown in Fig. 9(b). Despite increased uncertainty for the ultralow loss, our measured loss of HPSI 4H SiC is significantly lower than the values of our previous low-loss standards such as sapphire, which loss is greater than 1×10^{-4} between 55 and 330 GHz. This is consistent with the comparison of [7], which reported that at 137 GHz, tan $\delta_\perp = 6 \times 10^{-5}$ for HPSI 4H SiC and tan $\delta_\perp = 1.6 \times 10^{-4}$ for sapphire.

There are multiple arguments for HPSI 4H SiC to have the ultralow loss: 1) semi-insulating property due to high purity without impurity compensation or dipole formation, 2) wide bandgap with low intrinsic carrier concentration, 3) group-IV elements with covalent bonds and a small dipole with Si positively charged and C negatively charged, and 4) empirical perfection driven by high-volume power and optoelectronic applications. Based on the above arguments, it will be interesting to use the same methodology to characterize other wide-bandgap group-IV semiconductors such as diamond. However, presently, it is difficult to get large-area diamond with high quality and uniformity.

Theoretically, diamond and SiC have been predicted to have the lowest loss at millimeter-wave frequencies [16]. This is because both diamond and SiC can be low in thermal expansion, but high in bandgap, crystal symmetry, crystal perfectness, thermal conductivity, Debye temperature, and acoustic velocity. In this case, the lower limit of loss at room temperature is determined by the two-phonon absorption process, both acoustic phonons. In particular, the lower limit of 6H SiC at room temperature is predicted to be 5×10^{-5} at 150 GHz. Since the loss of 4H SiC should be comparable to that of

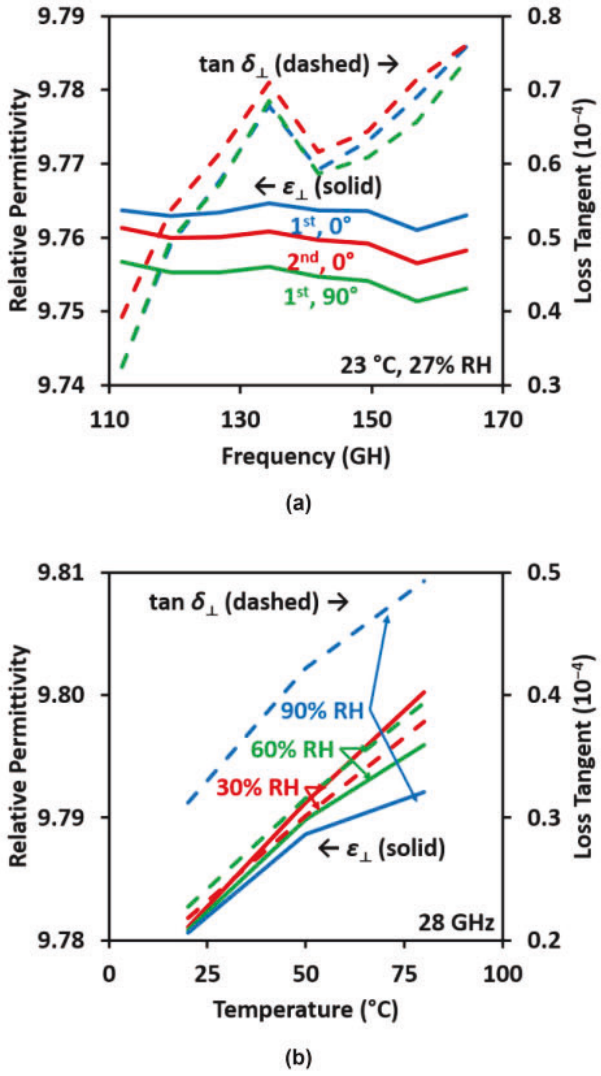

FIGURE 10. Ordinary permittivity $\varepsilon_\perp$ and loss tangent tan $\delta_\perp$ of 4H SiC measured on (a) two different quarters as well as the same quarter rotated 90° around the c axis and (b) the same quarter and orientation under different temperatures and humidities.

6H SiC, it implies that there may not be much room to further improve the loss of 4H SiC. It has also been predicted that the loss should have a cubic temperature dependence. However, this can be verified only by extending the temperature range of our measurements. Both $\varepsilon_\perp$ and tan $\delta_\perp$ of 4H SiC have been shown to have an exponential temperature dependence from 40 to 295 K at 40 GHz [6]. From the data, it is difficult to determine which polynomial fits the best at room temperature.

Fig. 10(a) shows that $\varepsilon_\perp$ and tan $\delta_\perp$ measured across the D band in the first and second quarters agree within 0.1% and 10%, respectively. The difference is comparable when the same quarter is rotated 90° around the c axis. This indicates that anisotropy is significant for tilt with respect to the c axis, but insignificant for rotation around the c axis. Fig. 10(b) shows the temperature and humidity dependence of $\varepsilon_\perp$ and tan $\delta_\perp$ measured on the same quarter at 28 GHz. It can be seen that at 20 °C and with the relative humidity increased from 30% to 90%, $\varepsilon_\perp$ decreases by less than 0.01%, whereas tan $\delta_\perp$ increases by less than 40%. At 80 °C and with the relative humidity increased from 30% to 90%, $\varepsilon_\perp$ decreases by less than 0.1%, whereas tan $\delta_\perp$ increases by less than 30%. This shows that while the permittivity of 4H SiC is relatively insensitive to humidity, its ultralow loss is sensitive to not only temperature, but also humidity. These characteristics are important considerations for using SiC in a harsh environment. However, the observed decrease in permittivity and increase in loss with increasing humidity may be due to surface adsorption instead of bulk absorption of water. In the future, these effects may be separated by measuring the humidity dependence of samples of different thicknesses.

To measure the extraordinary permittivity $\varepsilon_\parallel$, we previously used D-band SIWs fabricated at Cornell University on 100-μm-thick HPSI 4H SiC [12]. In this work, we use similarly designed D-band SIWs fabricated by the HRL foundry on 50-μm-thick HPSI 4H SiC using the T3 GaN-on-SiC 40-nm HEMT technology. From the measured β in the SIW, the extracted $\varepsilon_\parallel = 10.20 \pm 0.05$ is more precise and 0.1 lower than the previously reported value, even though the SIWs are measured on the same setup (Fig. 6) [10]. It can be seen in Fig. 2(b) that, similar to $\varepsilon_\perp$, $\varepsilon_\parallel$ is relatively constant across the D band. While the thinner substrate has little effect on β, it causes the insertion loss of the SIWs to increase from approximately 0.2 dB/mm in the previous case [10] to approximately 0.3 dB/mm in this work [Fig. 8(a)]. This is reasonable considering the loss of an SIW is inversely proportional to its thickness [3]. From (5), tan $\delta_\parallel$ is on the order of 0.01 across the D band. However, the tan $\delta_\parallel$ reported in this work is not the dielectric loss of HPSI 4H SiC, because presently the SIW loss is dominated by metal loss instead of dielectric loss [10]. Nevertheless, the $\varepsilon_\parallel$ and tan $\delta_\parallel$ obtained in this work have been used to design state-of-the-art D-band power amplifiers with monolithic integration of SiC SIWs and GaN HEMTs [17], [18]. The amplifiers were also fabricated by the HRL foundry on 50-μm-thick 4H SiC using its T3 GaN-on-SiC 40-nm HEMT technology with first-pass success, validating the accurate models of material and device characteristics.

Fig. 11 shows the measured temperature dependence of $\varepsilon_\perp$, $\varepsilon_\parallel$, tan $\delta_\perp$, and tan $\delta_\parallel$ across the D band. It can be seen that they all increase slightly with increasing temperature. In particular, $\varepsilon_\perp = 9.77 \times (1 + 6 \times 10^{-5}\ \Delta T)$, $\varepsilon_\parallel = 10.20 \times (1 + 1 \times 10^{-4}\ \Delta T)$, tan $\delta_\perp = 7 \times 10^{-5} \times (1 + 1 \times 10^{-2}\ \Delta T)$, and tan $\delta_\parallel = 0.01 \times (1 + 1 \times 10^{-3}\ \Delta T)$, where ΔT is the temperature increase from room temperature in °C. Thus, both $\varepsilon_\perp$ and $\varepsilon_\parallel$ have a relatively weak temperature coefficient on the order of 10^{-4} /°C, whereas tan $\delta_\perp$ and tan $\delta_\parallel$ have relatively high temperature coefficients on the order of 10^{-2} /°C and 10^{-3} /°C, respectively. The temperature coefficient of tan $\delta_\parallel$ is consistent with the temperature coefficient of metal resistivity, which is on the order of 10^{-3} /°C [19].

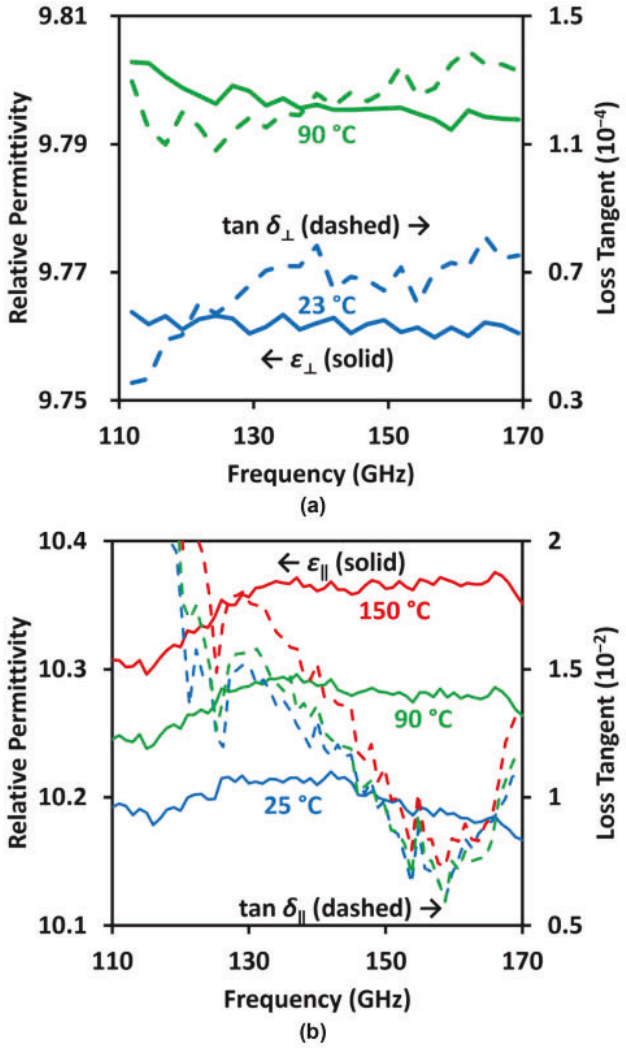

FIGURE 11. Temperature-dependent (a) $\varepsilon_\perp$, tan $\delta_\perp$ and (b) $\varepsilon_\parallel$, tan $\delta_\parallel$ of 4H SiC across the D band.

IV. CONCLUSION

In this work, we measured $\varepsilon_\perp$, $\varepsilon_\parallel$, tan $\delta_\perp$ and tan $\delta_\parallel$ with order-of-magnitude-improved precision. We found $\varepsilon_\perp$ and $\varepsilon_\parallel$ to be constant across most millimeter-wave frequencies, whereas tan $\delta_\perp$ to increase linearly with frequency. This seems reasonable, because, without ionic/electronic conduction or molecular dipole relaxation, the remaining atomic relaxation between the atomic nucleus and core electrons is above terahertz frequencies [20]. The fact that $\varepsilon_\perp < \varepsilon_\parallel$ also seems reasonable, because the c plane of a hexagonal semiconductor is the densest packed. The linear frequency dependence of tan $\delta_\perp$ agrees with the 2-phonon absorption mechanism [16].

REFERENCES

[1] J. B. Casady and R. W. Johnson, "Status of silicon carbide (SiC) as a wide-bandgap semiconductor for high-temperature applications: A review," *Solid-State Electron.*, vol. 39, no. 10, pp. 1409–1422, Oct. 1996, doi: 10.1016/0038-1101(96)00045-7.

[2] K. Momma and F. Izumi, "*VESTA 3* for three-dimensional visualization of crystal, volumetric and morphology data," *J. Appl. Crystallogr.*, vol. 44, no. 6, pp. 1272–1276, Dec. 2011, doi: 10.1107/S0021889811038970.

[3] D. M. Pozar, *Microwave Engineering*, 4th ed. Hoboken, NJ, USA: Wiley, 2012.

[4] J. M. Dutta, G. Yu, and C. R. Jones, "Dielectric losses in SiC at millimeter wavelengths," in *Proc. Joint 31st Int. Conf. Infrared Millimeter Waves 14th/Int. Conf. Teraherz Electron.*, Shanghai, China, 2006, p. 411, doi: 10.1109/ICIMW.2006.368619.

[5] S. Chen, M. N. Afsar, and D. Sakdatorn, "Dielectric-parameter measurements of SiC at millimeter and submillimeter wavelengths," *IEEE Trans. Instrum. Meas.*, vol. 57, no. 4, pp. 706–715, Apr. 2008, doi: 10.1109/TIM.2007.913594.

[6] J. G. Hartnett, D. Mouneyrac, J. Krupka, J.-M. Le Floch, M. E. Tobar, and D. Cros, "Microwave properties of semi-insulating silicon carbide between 10 and 40 GHz and at cryogenic temperatures," *J. Appl. Phys.*, vol. 109, no. 6, Mar. 2011, Art. no. 064107, doi: 10.1063/1.3561431.

[7] C. R. Jones, J. Dutta, G. Yu, and Y. Gao, "Measurement of dielectric properties for low-loss materials at millimeter wavelengths," *J. Infrared, Millimeter, THz Waves*, vol. 32, no. 6, pp. 838–847, Jun. 2011, doi: 10.1007/s10762-011-9795-4.

[8] M. Naftaly, J. F. Molloy, B. Magnusson, Y. M. Andreev, and G. V. Lanskii, "Silicon carbide—A high-transparency nonlinear material for THz applications," *Opt. Exp.*, vol. 24, no. 3, pp. 2590–2595, Feb. 2016, doi: 10.1364/OE.24.002590.

[9] A. T. Tarekegne, B. Zhou, K. Kaltenecker, K. Iwaszczuk, S. Clark, and P. U. Jepsen, "Terahertz time-domain spectroscopy of zone-folded acoustic phonons in 4H and 6H silicon carbide," *Opt. Exp.*, vol. 27, no. 3, pp. 3618–3628, Feb. 2019, doi: 10.1364/OE.27.003618.

[10] L. Li, S. Reyes, M. J. Asadi, P. Fay, and J. C. M. Hwang, "Extraordinary permittivity characterization of 4H SiC at millimeter-wave frequencies," *Appl. Phys. Lett.*, vol. 123, no. 1, Jul. 2023, Art. no. 012105, doi: 10.1063/5.0148623.

[11] A. L. Cullen and P. K. Yu, "The accurate measurement of permittivity by means of an open resonator," *Proc. Roy. Soc. Lond. A, Math. Phys. Sci.*, vol. 325, no. 1563, pp. 493–509, Dec. 1971, doi: 10.1098/rspa.1971.0181.

[12] M. J. Asadi et al., "SiC substrate-integrated waveguides for high-power monolithic integrated circuits above 110 GHz," in *Proc. IEEE MTT-S Int. Microw. Symp.*, Atlanta, GA, USA, 2021, pp. 669–672, doi: 10.1109/IMS19712.2021.9574845.

[13] R. B. Marks, "A multiline method of network analyzer calibration," *IEEE Trans. Microw. Theory Techn.*, vol. 39, no. 7, pp. 1205–1215, Jul. 1991, doi: 10.1109/22.85388.

[14] S. Hu et al., "THz-wave propagation characteristics of TSV-based transmission lines and interconnects," in *Proc. 60th Electron. Compon. Technol. Conf.*, Las Vegas, NV, USA, 2010, pp. 46–50, doi: 10.1109/ECTC.2010.5490880.

[15] F. Xu and K. Wu, "Guided-wave and leakage characteristics of substrate integrated waveguide," *IEEE Trans. Microw. Theory Techn.*, vol. 53, no. 1, pp. 66–73, Jan. 2005, doi: 10.1109/TMTT.2004.839303.

[16] B. M. Garin, "Lower loss limits at millimeter and terahertz ranges," in *Conf. Dig. Joint 29th Int. Conf. Infrared Millimeter Waves/12th Int. Conf. THz Electron*, Karlsruhe, Germany, 2004, pp. 393–394, doi: 10.1109/ICIMW.2004.1422127.

[17] L. Li, P. Fay, and J. C. M. Hwang, "A D-band frequency-doubling traveling-wave amplifier through monolithic integration of a SiC SIW and GaN HEMTs," *IEEE J. Microwaves*, vol. 4, no. 1, pp. 158–166, Jan. 2024, doi: 10.1109/JMW.2023.3340117.

[18] L. Li, T. Li, P. Fay, and J. C. M. Hwang, "AD-band traveling-wave amplifier by embedding GaN HEMTs as current probes in a SiC SIW," in *Proc. IEEE/MTT-S Int. Microw. Symp.*, Washington, DC, USA, 2024, pp. 686–689.

[19] J. Bardeen, "Electrical conductivity of metals," *J. Appl. Phys.*, vol. 11, no. 2, pp. 88–111, Feb. 1940, doi: 10.1063/1.1712751.

[20] A. K. Jonscher, "Dielectric relaxation in solids," *J. Phys. Appl. Phys.*, vol. 32, no. 14, pp. R57–R70, Jul. 1999, doi: 10.1088/0022-3727/32/14/201.

TIANZE LI (Student Member, IEEE) received the B.S. degree in physics from the University of California, Los Angeles, CA, USA, in 2022, and the M.S. degree in materials science and engineering from Cornell University, Ithaca, NY, USA, in 2024, where she is currently working toward the Ph.D. degree in electrical and computer engineering. Her research interests include millimeter-wave materials, devices, and circuits. She was the recipient of the ARFTG Roger Pollard Student Fellowship in microwave measurement in 2024.

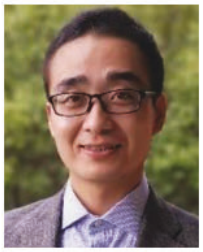

LEI LI (Member, IEEE) received the B.S. degree in electrical engineering from the University of Science and Technology of China, Hefei, China, in 2016, the M.S. degree in electrical engineering from Lehigh University, Bethlehem, PA, USA, in 2018, and the Ph.D. degree in electrical engineering from Cornell University, Ithaca, NY, USA, in 2023. He is currently with Cornell University as a Postdoctoral Fellow. His research interests include millimeter-wave materials, devices, and circuits. He was the recipient of the IEEE MTT-S graduate fellowship in 2021 and the ARFTG Best Student Paper Award in 2023.

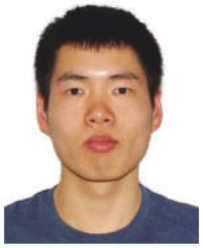

XIAOPENG WANG (Member, IEEE) received the B.S. degree in information engineering from Xi'an Jiaotong University, Xi'an, China, in 2015, the M.S. degree in electrical engineering from Lehigh University, Bethlehem, PA, USA, in 2017, and the Ph.D. degree in electrical and computer engineering from Cornell University, Ithaca, NY, USA, in 2024. He is currently with Cornell University as a Postdoctoral Fellow. His research interests include millimeter-wave materials, devices, and circuits. He was the recipient of the ARFTG Roger Pollard Student Fellowship in Microwave Measurement in 2022.

JAMES C. M. HWANG (Life Fellow, IEEE) received the B.S. degree in physics from the National Taiwan University, Taipei, Taiwan, and the M.S. and Ph.D. degrees in materials science and engineering from Cornell University, Ithaca, NY, USA. He spent most of his academic career with Lehigh University, Bethlehem, PA, USA, after years of industrial experience with IBM, Yorktown Heights, NY, USA; Bell Labs, Murray Hill, NJ, USA; GE, Syracuse, NY, USA; and GAIN, Somerville, NJ, USA. He is currently a Professor with the Department of Materials Science and Engineering, Cornell University. He cofounded GAIN and QED, Bethlehem, PA, USA; the latter became the public company IQE. He was a consultant for the U.S. Air Force Research Laboratory, Dayton, OH, USA, and a Program Officer for GHz-THz Electronics with the Air Force Office of Scientific Research, Arlington, VA, USA. He was an IEEE Distinguished Microwave Lecturer. He is an editor for IEEE TRANSACTIONS ON MICROWAVE THEORY AND TECHNIQUES. He has worked on microwave materials, devices, and circuits for decades. He was the recipient of many honors and awards, including the IEEE Lester F. Eastman Award for outstanding achievement in high-performance semiconductor devices.

SHANA YANAGIMOTO received the B.S. and M.S. degrees in bio engineering from Osaka University, Osaka, Japan, in 2015 and 2017, respectively. In 2017, he was employed by Panasonic Corporation, Osaka, Japan, as a Development Hardware Engineer involving on board charger for electric vehicle. In 2021, he joined EM Labs, Inc., Kobe, Japan, as a Millimeter-Wave Engineer.

YOSHIYUKI YANAGIMOTO received the B.S. and M.S. degrees in physics from Kyoto University, Kyoto, Japan, in 1983 and 1985, respectively. In 1985, he was employed by Hewlett Packard, Inc. (later split to Agilent Technologies, Inc., and then Keysight Technologies, Inc.), Kobe, Japan, as a Research and Development Hardware Engineer involving electronic measurement instruments. After serving as the Research and Development Section Manager, he became the Senior Marketing Manager of the Component Test Division in 2004. Since then, he has been the Founder and CEO of EM labs, Inc., Kobe, Japan.